RSC Advances

ROYAL SOCIETY OF CHEMISTRY

www.rsc.org/advances

Constructing metal-free polyimide/g-C_3N_4 with high photocatalytic activity under visible light irradiation

Yan Gong, Hongtao Yu*, Shuo Chen, Xie Quan

Key Laboratory of Industrial Ecology and Environmental Engineering (Ministry of Education, China), School of Environmental Science and Technology, Dalian University of Technology, Dalian 116024, China

Correspondence should be addressed to Hongtao Yu: Hongtao Yu@dlut.edu.cn

Abstract

A novel metal-free polyimide (PI)/g-C_3N_4 heterojunction has been prepared through a sonochemical approach. The PI/g-C_3N_4 composite exhibits an extraordinary high photogenerated carriers separation efficiency and sequentially a high-efficiency photocatalytic capability in degradation of 2,4-dichlorophenol (2,4-DCP) under visible light irradiation. In particular, the optimum photocatatlytic activity of the PI/g-C_3N_4 composites with weight ratio of PI at 30% is almost 3.8 times as high as that over g-C_3N_4. Furthermore, it was found by experimental analysis and density functional theory (DFT) calculations that the superior photocatalytic performance of the composites can be attributed to the facile band alignment and different electronic structure of g-C_3N_4 and PI components in the heterojunction for efficient charge separation and transfer.

Introduction

Graphitic carbon nitride (g-C_3N_4) has been regarded as promising metal-free visible-light polymeric photocatalyst for environmental applications owing to their abundance, stability, and chemical tenability [1, 2]. However, the photocatalytic performance of g-C_3N_4 has been restricted by the low efficiency, mainly due to the fast photogenerated carrier recombination.

To overcome this issue, efforts have been made for the improvement of photoinduced carrier separation ability, such as doping with metal [3, 4] or nometal element [5, 6], texture modification [7-10], and constructing heterojuction [11-15]. Among these strategies, constructing heterostructured photocatalysts composed of multi-semiconductors offers a promising approach to promote charge separation. In this composite system, the interface junction provides efficient charge separation to suppress the photogenerated carrier recombination, owning to the electric field in the interface area. And the separated charge carriers can migrate to the surface active sites around the interface area or diffuse to the bulk part of the semconductor to participate in the reaction. Up to now, several g-C_3N_4-based heterojunctions have been studied by coupling of g-C_3N_4 with other types of inorganic [16-19] and organic semiconductors [20-22]. However, the coupled inorganic components in these reported heterojunctions are usually metal-containing, which raise the potential toxic metal leaching and the associated secondary contamination [23], besides the organic

semiconductors often exhibit less efficiency photocatalytic activities. Therefore, an alternative metal-free component with high photocatalytic capability is desired for construting an efficient and environmentally friendly photocatalyst with g-C_3N_4. An ideal component must meet two requirements, one is an appropriate band position to form heterojunction with g-C_3N_4 for facilitating the separation of electrons and holes at the interface, the other is high efficient charge separation and transfer ability for the bulk part of the component since it is also a crucial factor for constructing an efficient photocatalyst. Unfortunately, previous reports cannot fully integrate the above-mentioned merits. So it is urgent demand to exploit a proper photocatalyst to fulfill the aforementioned requirements. Among various metal-free photocatalysts, the polyimide (PI) is an ideal candidate [24, 25]. Because of the introducing electron-deficient pyromellitic dianhydride (PMDA) monomer into the network of g-C_3N_4, the valence band position and conduction band position of PI are both lower than that of g-C_3N_4. And this band offset may provide an effective approach to construct a heterojunction based on g-C_3N_4 to cover the shortage of g-C_3N_4 for improved photocatalysis. In addition, owing to the different electronic structure between g-C_3N_4 and PI, PI exhibits enhanced photogenerated charge separation capability compared with g-C_3N_4. Thus the separated charge carriers from the interface junction area can rapidly transfer to the surface of PI to participate in the reaction when both of PI and g-C_3N_4 are integrated together as a heterojunction. However, to the best of our knowledge, there is no study on this novel metal-free heterostructure photocatalyst.

In this work, we synthesized the PI/g-C_3N_4 metal-free heterojunction via a simple sonication method. The composite photocatalyst was then carefully examined by experimental analyses and theoretical calculations. Benefiting from the suitable band position features, the as-prepared PI/g-C_3N_4 composite exhibited significantly enhanced photogenerated charge separation ability and photocatalytic activity for the degradation of 2, 4-DCP under visible light irradiation.

2. Experimental Details

2.1 Preparation of g-C_3N_4 and PI

All chemicals used in the experiments were reagent grade and without further purification. Pure g-C_3N_4 powders were prepared by calcining melamine in a muffle furnace. In details, 5 g of melamine was placed in an alumina crucible with a loose cover and then heated to 550 ℃ with a heating rate of 5 ℃/min and held for 4 h. After cooling to room temperature, g-C_3N_4 was collected and ground into powder. The PI was synthesized by heating the mixture of Melem and PMDA with equal molar ratio at 598 K for 4 h at a heating rate of 7 K/min [24]. The obtained solid was washed with water, the final product was then filtered and dried at 60 ℃ for 12 h.

2.2 Construction of PI/g-C_3N_4 composite photocatalyst

The PI/g-C_3N_4 composite photocatalysts were fabricated via a simple sonication and thermal treatment approach. In a typical procedure, the as-prepared g-C_3N_4 powder (0.1 g) was dispersed in 100 mL of ethanol through sonication. Then a certain amount of PI powder was added into the above solution and stirred for 12 h at room

temperature. the resulting powder was washed with ultrapure water for several times, and dried under vacuum at 100 °C for 12 h to obtain the PI/g-C_3N_4 samples. The counterpart g-C_3N_4 was also synthesized without adding the PI.

2.3 Characterizations

The crystal structure of the samples was investigated by using an X-ray diffractometer (XRD, Shimadzu LabX XRD-6000). The morphologies of the sample were observed by transmission electron microscopy (TEM FEI-Tecnai G^2 F30). The surface functional groups was measured by Fourier transform spectrophotometer (FT-IR, VERTEX 70, Bruker) with KBr as the reference sample. And the optical absorption properties was investigated by diffuse reflectance spectra (DRS) using a UV–vis spectrophotometer (Shimadzu, UV-2450). The N_2 adsorption-desorption isotherms were obtained at 77 K with a Quadrasorb instrument. X-ray photoelectron spectroscopy (XPS) measurements were performed on a Thermo Scientific ESCALAB 250 instrument with Al Kα source. The Electrochemical and photoelectrochemical performances were tested on a CHI 660B electrochemical system (Shanghai, China) using a standard three-electrode cell (working electrode, Pt counter electrode and standard calomel electrode (SCE), in 0.5 M Na_2SO_4 solution). The working electrode was prepared as follows: 5 mg of as-prepared photocatalyst was suspended in 1 mL dimethylformamide (DMF) to produce slurry, which was then dip-coated onto a 2 cm x 2 cm indium-tin oxide (ITO) glass. The electrode was then annealed at 200 °C for 2 h under argon flow. Electrochemical impedance spectra (EIS) were measured at 0V (vs. SCE). A sinusoidal ac perturbation of 5 mV was applied to the electrode over the frequency range of 10^{-2}–10^5 Hz.

2.4 Photocatalytic capability

The photocatalytic activity of the PI/g-C_3N_4 composite was evaluated by degradation of 2, 4-DCP aqueous solution under visible light irradiation. A 300W high pressure xenon lamp (CHF-XM35-300W, Beijing Changtuo Co.) was used as the light source, and wavelengths below 420 nm were cut off by an optical filter for visible light. A Radiometer of model FZ-A (Photoelectric Instrument Factory Beijing Normal University) was used to ensure the incident visible-light intensity was 100 mW/cm^2. Prior to irradiation, 50 mg photocatalyst was added into 50 ml 2, 4-DCP solutions (10 mg/L) and the mixture was stirred in the dark for 1h to achieve adsorptive equilibrium. After desired intervals, samples were collected and centrifuged to remove photocatalyst for subsequent analysis. The concentration of 2, 4-DCP was measured on a high performance liquid chromatography (Shimadzu, LC10A HPLC). A Discovery C18 column was used, and the analysis was carried out with a 70/30 (v/v) methanol/water mobile phase at a flow rate of 1.0 mL/min. To investigate the active species generated in the photocatalytic degradation process, the experiments of free radicals (hydroxyl radical, hole and $\bullet O^{2-}$) capture were carried out by Isopropanol (IPA), ethylenediamine tetraacetic acid disodium salt (EDTA-2Na) and N_2, respectively.

2.5 DFT calculations

All calculations were performed at the DFT level within the $Dmol^3$ program, using the DNP basis set. We optimize the g-C_3N_4 and PI structures with a cluster

model by using the BLYP method without any symmetry constraints. And the highest occupied molecular orbital (HOMO) and lowest unoccupied molecular orbital (LUMO) were analyzed on the basis of the optimized results.

3. Results and discussion

3.1 Structure and Morphology of PI/g-C_3N_4 photocatalysts

The crystal structure and phase composition of the obtained samples were characterized by XRD and the resulting patterns are shown in Figure 1. The XRD pattern for g-C_3N_4 shows two distinct diffraction peaks at 13.2° and 27.4°, corresponding to the (100) and (002) peaks of the graphitic phase, respectively[26]. And the XRD pattern for PI exhibits several sharp peaks in the range of 10-30°, implying the high crystallinity. Two peaks at 2θ=19.0° and 29.6° are assigned to π, π-stacking of PMDA units [27] and donor-acceptor interaction between melem and PMDA units [28] respectively. After PI loading, two characteristic diffraction peaks of PI can be detected in the PI/g-C_3N_4 samples, and these two peak's intensity increases with the increase in PI loading amount. This result confirmed the co-existence of g-C_3N_4 and PI in the composite, and no impurity phases are detected indicating that the crystal phases of g-C_3N_4 and PI do not change after hybridization.

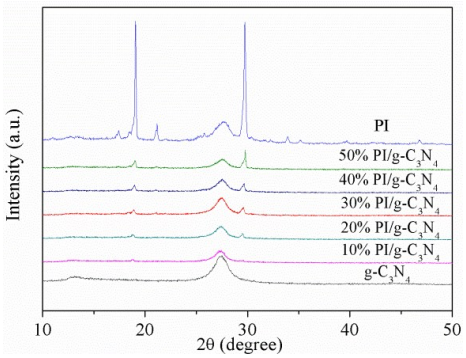

Figure 1. XRD patterns of PI, g-C_3N_4, and PI/g-C_3N_4

The existence of PI can be further confirmed by the FTIR (Figure 2a and b). In the case of g-C_3N_4, the board peaks between 3000 and 3500 cm^{-1} corresponded to the uncondensed amine groups and surface adsorbed water molecules. The peaks at 1251, 1325 and 1419 cm^{-1} are attributable to the aromatic C–N stretching vibration modes, while the 1571, and 1639 cm^{-1} are contributed to the C=N typical stretching vibration modes. In addition, the characteristic breathing mode of triazine units at 810 cm^{-1} is observed [29]. For the PI, the peaks around 1774, 1725, and 725 cm^{-1} are attributed to the stretching and bending vibrations of the C=O bond in the PMDA moiety of PI [30], while the band around 1375 cm^{-1} is assigned to the stretching vibration of C-N-C in the five-membered imide rings [31]. In the case of PI/g-C_3N_4 composite, Two sharp absorption peaks at 725 and 1775 cm^{-1} for PI are observed in PI/g-C_3N_4 as depicted in Figure 2b, indicating the existence of PI in the PI/g-C_3N_4 composite. Noteworthy, these two sharp peaks can be observed more and more apparent as the loading amount

of PI increasing, indicating that the PI is homogenously immobilized on the surface of the g-C_3N_4 and successfully coupled with g-C_3N_4.

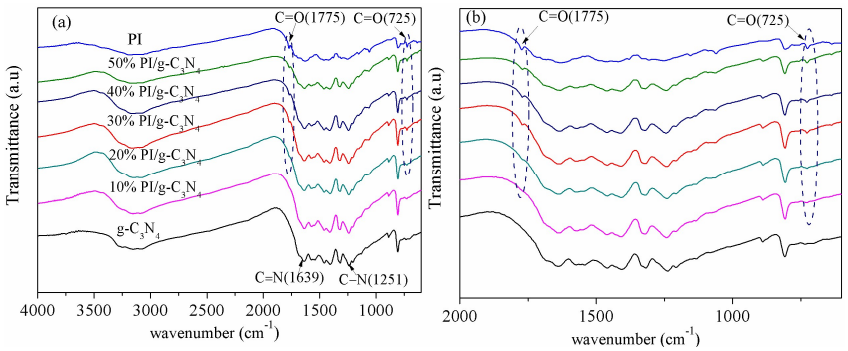

Figure 2. (a) FT-IR spectra of g-C_3N_4, PI and PI/g-C_3N_4 photocatalysts and (b) enlarged view of FTIR spectra (a).

TEM was carried out to study the morphological and structural features of the PI/g-C_3N_4 samples along with the g-C_3N_4 and PI. As shown in Figure 3a, the g-C_3N_4 is composed of smooth thin layer structure, where as the PI consist of interconnected particles with sizes of about 50 nm (Figure 3b). Figure 3c shows the morphology of PI/g-C_3N_4, it can be seen that the PI particles are tightly attached on the surface of g-C_3N_4 with intimate contacts, both of which are integrated together as a heterostructure. This result gives a more straightforward evidence of the successful formation of the PI/g-C_3N_4 heterostructure.

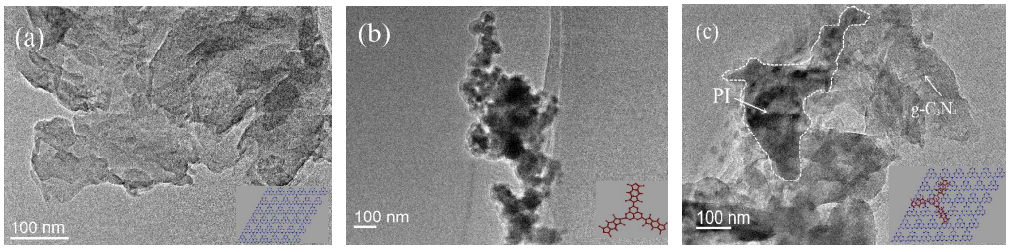

Figure 3. TEM images of (a) pure g-C_3N_4, (b) pure PI, (C) PI/g-C_3N_4

The specific surface areas of the g-C_3N_4 and PI/g-C_3N_4 composite were investigated by nitrogen adsroption-desorption analysis. As shown in Figure 4, the Brunauer-Emmett-Teller (BET) surface area of the g-C_3N_4 and PI/g-C_3N_4 were calculated to be ca. 22.5 m^2 g^{-1} and 23.1 m^2 g^{-1}, respectively. The introduction of PI into the matrix of g-C_3N_4 shows limited influence on the BET surface area of the samples. This result indicates that the surface area may not be the primary factor accounting for the different photocatalytic preformances of the g-C_3N_4 and PI/g-C_3N_4.

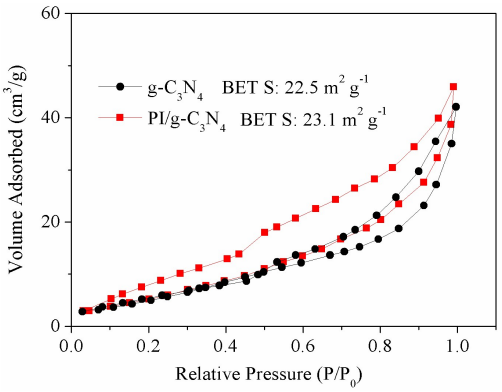

Figure 4. Nitrogen adsorption–desorption isothermsof g-C_3N_4 and PI/g-C_3N_4

3.2. Optical absorption and photoelectric properties

The optical properties of heterojunction photocatalysts were shown in Figure 5. Both of g-C_3N_4 and PI show obvious visible light response ability. g-C_3N_4 exhibits an absorption edge at around 460 nm while that of PI is located at 480 nm. The band gaps of as-synthesized g-C_3N_4 and PI determined from the intercept of the tangents to the plots of $(\alpha h\nu)^2$ vs. photon energy are 2.8 eV and 2.85 eV, respectively. As expected, the absorption edges of PI/g-C_3N_4 composite are located at the ranges between g-C_3N_4 and PI, which indicates that the PI/g-C_3N_4 composite can be used as excellent visible light photocatalysts.

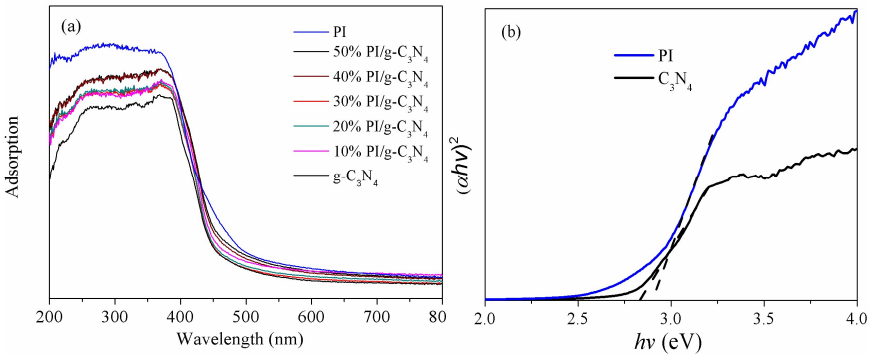

Figure 5. (a) UV–vis diffuse reflectance spectra of g-C_3N_4, PI and PI/g-C_3N_4 photocatalysts and (b) the corresponding Tauc plot

Photoelectrochemical test is used to evaluate the efficiency of photogenerated charge separation. The transient photocurrent responses of a photocatalyst may correlate with the separation efficiency of photogenerated carriers. The transient photocurrent responses of the g-C_3N_4 and PI/g-C_3N_4 were recorded for several on-off cycles under visible-light irradiation and depicted in Figure 6. It can be seen that the photocurrent of the PI/g-C_3N_4 electrode was ~0.4 μA/cm^{-2}, which is about four times as high as that of the g-C_3N_4 electrode. This photocurrent enhancement of the PI/g-C_3N_4 photocatalyst indicated an enhanced photoinduced electrons and holes separation, which could be attributed to the synergetic effect of the formation of PI/g-C_3N_4 heterojunction promoting the charges separation.

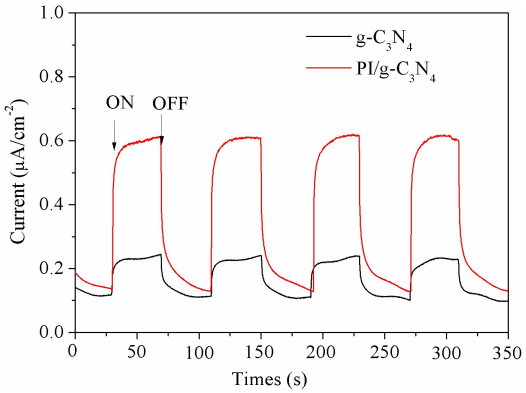

Figure 6. The transient photocurrent density responses of pure g-C_3N_4 and PI/g-C_3N_4 samples electrodes with light on/off cycles under visible light irradiation

3.3 Mechanism of enhancement of photogenerated charge separation

It is well know that a facile band alignment plays a key role in a heterojunction photocatalyst with high photocatalytic ability. To exploits the band position of the PI and g-C_3N_4, XPS valence band spectra was used to estimate the positions of valence band maximum (VBM). As shown in Figure 7a, the VBM of PI and g-C_3N_4 are revealed to be 2.16 and 1.67 eV, respectively, the PI possesses a more positive valence band edge by 0.49 eV than that of the g-C_3N_4. Combing the result of XPS valence spectra (Figure 7a) and the band-gap values extrapolated by UV/Vis spectra (Figure 5b), we deduced the band alignments of PI /g-C_3N_4 heterojunction can be drawn as shown in Scheme 1. By virtue of this staggered band feature of the PI/g-C_3N_4, photogenerated electrons would migrate from g-C_3N_4 to PI, and holes would be transported in the opposite direction at the interface. The potential difference is the main driving force for efficient charge separation and transfer. Such charge migration processes is in favour of overcoming the high dissociation barrier of the Frenkel exciton and endows the PI/g-C_3N_4 photocatalyst with efficient photogenerated carrier separation capability.

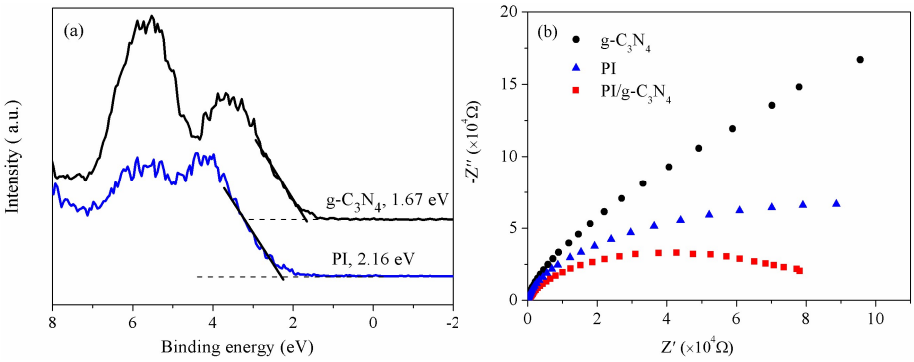

Figure 7. (a) VB XPS spectra of PI and g-C_3N_4 and (b) EIS Nyquist plots of the g-C_3N_4, PI and PI/g-C_3N_4 photocatalysts under visible light irridation

Besides the well-matched bandposition, the intrinsic electronic strucrure of semiconductor is also a key factor for an efficient photocatalyst. To gain a deeper

understanding of the different electronic strucrures of PI and g-C_3N_4, density functional theory (DFT) calculations were performed to analyze the electronic structures of PI and g-C_3N_4 with cluster models. As depict in Scheme 1, the HOMO and LUMO of g-C_3N_4 are composed of 2p orbitals of heterocyclic N atoms and the C-N bond orbitals respectively, both the HOMO and LUMO are located on the melem moiety. Noteworthy, the HOMO of PI is located at the melem moiety position, but the LUMO of PI has changed from the melem to the PMDA moiety, and this result is in agreement with a previous report [26]. As we know, the HOMO and LUMO located in different parts favours the spatial charge separation and benefits the photocatalysis process[32,33], thus PI present higher pohotogenerated charge separation capability than that of g-C_3N_4. To verify this hypothesis, electrochemical impedance spectroscopy (EIS) was used to investigate the photogenerated charge separation process. It is accepted that a smaller arc radius of the EIS Nyquist plot corresponds to an effective separation of photogenerated electron-hole pairs and fast interfacial charge transfer. The EIS Nyquist plots of PI and g-C_3N_4 and PI/g-C_3N_4 electrodes under visible light irradiation are shown in Fig. 7b. The arc radius on EIS Nyquist plot of PI/g-C_3N_4 heterojunction is smaller than that of g-C_3N_4 and PI. This suggests that the PI/g-C_3N_4 owns a more effective photogenerated carrier separation and fast interfacial charge transfer capability. In addition, the arc radius on EIS Nyquist plot of PI is smaller than that of g-C_3N_4 which demonstrates that the PI shows higher charge carrier separation ability than that of g-C_3N_4. These results indicate dramatically enhanced separation and transfer efficiency of photogenerated electron/hole pairs in PI/g-C_3N_4 is attributed to the formation of this novel heterojunction accompany with the high charge separation ability of PI. Thus the PI/g-C_3N_4 heterojunction photocatalyst anticipates high photocatalytic activity under visible light irradiation.

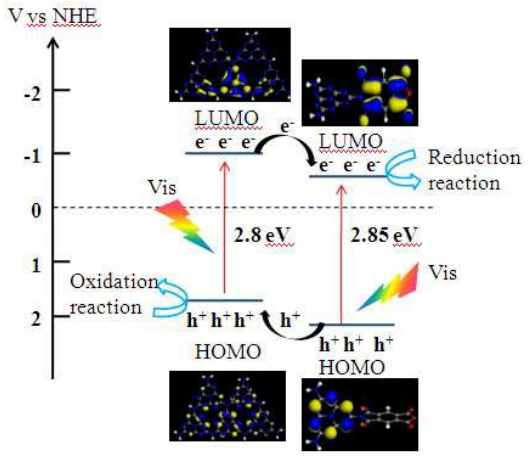

Scheme 1. Schematic drawing illustrating the energy-level configuration and the mechanism of charge separation over PI/g-C_3N_4 photocatalysts under visible light irradiation

3.4 Photocatalytic activity of the PI/g-C_3N_4 photocatalysts

The photocatalytic activity of the g-C_3N_4 and PI/g-C_3N_4 were therefore evaluated by photodegradation of 2,4-DCP under visible light irradiation. Figure 8a shows the

2,4-DCP photodegradation on g-C_3N_4 and PI/g-C_3N_4 photocatalysts with different PI content under visible-light irradiation. Control experiment revealed that the 2,4-DCP showed high photostability under visible light irradiation. All PI/g-C_3N_4 photocatalysts exhibited markedly higher photocatalytic activity than that of g-C_3N_4 under visible-light irradiation. With the increase of PI content from 10 wt% to 30 wt%, the removal rate of 2,4-DCP was increased gradually from 52% to 98%. However, when the loading amount exceeds 30 wt%, the photocatalytic activities of PI/g-C_3N_4 composites decreased as the amount of PI increased. This implies that the amount of PI has great influences on the photocatalytic activity of PI/g-C_3N_4 photocatalyst. And the 30 wt% PI/g-C_3N_4 exhibited the highest photocatalytic activity for degradation of 2,4-DCP among these PI/C_3N_4 composites. The photocatalytic degradation process follows pseudo-first-order kinetics, The corresponding kinetic constants (k) were calculated and depicted in Figure 8b. Under the same experimental conditions, the kinetic constant of 2,4-DCP degradation with 30% PI/g-C_3N_4 was 3.8 times as large as that of pristine g-C_3N_4, which showed that the introduction of PI could enhance the photocatalytic capability of g-C_3N_4 efficiently under visible light irradiation. This significant enhancement on photocatalytic performance was attributed to the facile band alignment of the PI and g-C_3N_4 which is of great benefit for the photogenerated charge separation. Meanwhile, both PI and g-C_3N_4 are metal-free photocatalysts which can reduce the secondary contamination during photocatalysis process. Thus this hetrojunction composite can be used as a high-efficiency photocatalyst for environmental remediation in future.

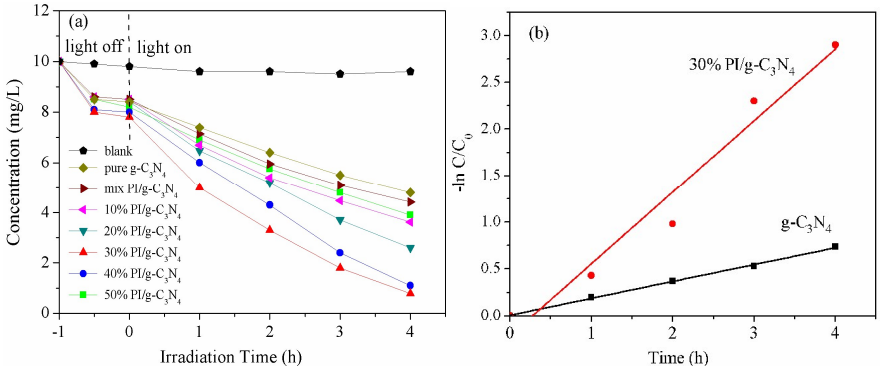

Figure 8. (a) Photocatalytic activities of as-prepared photocatalysts for 2,4-DCP degradation under visible-light irradiation and (b) Apparent rate constants for the photocatalytic degradation of 2,4-DCP

3.5 Stability test of PI/g-C_3N_4 photocatalyst

Repeatability experiments of 2,4-DCP degradation over PI/g-C_3N_4 were conducted to evaluate the photocatalytic stability of the PI/g-C_3N_4 heterojunction. Figure 9 revealed that the degradation efficiency of 2,4-DCP show no obvious decrease after six consecutive experiments, illustrating that PI/g-C_3N_4 composite possesses excellent visible-light photocatalytic stability. The high stability of PI/g-C_3N_4 composite demonstrates that it can serve as a high efficient visible-light

response photocatalyst.

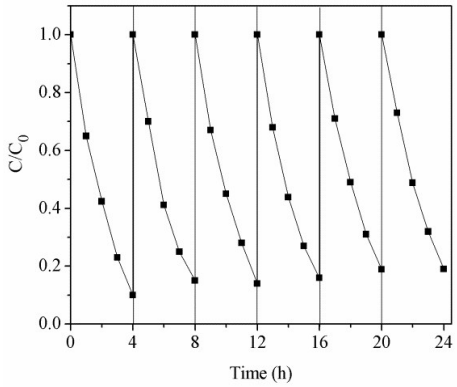

Figure 9. Stability test of PI/g-C_3N_4 under visible light irradiation

3.6 Investigation of reactive species

In order to investigate photocatalytic mechanisms of the PI/g-C_3N_4 photocatalyst, several scavengers were used to explore the reactive species in the process of photocatalytic reaction. The EDTA-2Na was used as hole radical scavenger and Isopropanol (IPA) was employed to impair the hydroxyl radical (•OH), and the purging N_2 was applied to reduce the superoxide radical ($\bullet O^{2-}$) [22, 29], respectively. As shown in Figure 10, the photocatalytic activity of PI/g-C_3N_4 shows no obvious change by the addition of IPA, while has a remarkably decrease by the addition of EDTA-2Na and purging N_2 gas, indicating that both $\bullet O^{2-}$ and photogenerated holes might be the main oxidative species.

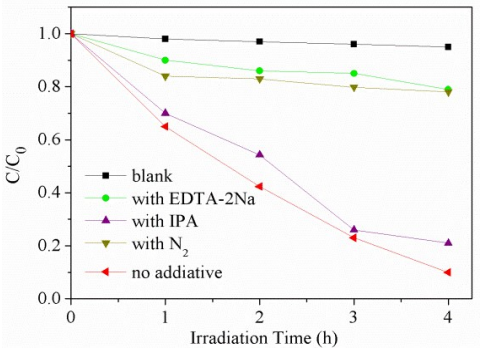

Figure 10. Reactive specie trapping experiments of PI/g-C_3N_4 under visible light irradiation

4. Conclusions

In this work, a metal-free PI/g-C_3N_4 heterojunction has been successfully constructed by using a simple a sonochemical method. The PI/g-C_3N_4 heterojunction exhibits superior photocatalytic activity of 2,4-DCP degradation under visible light irradiation, and the kinetic constant over PI/g-C_3N_4 is about 3.8 times as high as that of g-C_3N_4. The significant enhancement on photocatalytic performance was attributed to not only the facile band alignment of the PI and g-C_3N_4 which promoting the separation and transfer of photogenerated carriers, but also the rapid photoinduced charge separation efficiency of PI in PI/g-C_3N_4 composite. This work can provide

important inspirations for developing of novel photocatalytic materials.

Acknowledgments

The work was supported by the National Natural Science Foundation of China (NSFC-JST 21261140334)

References

[1] X. C. Wang, K. Maeda, A. Thomas, K. Takanabe, G. Xin, K. Domen, M. Antonietti, Nat. Mater. 8 (2009) 76

[2] J. Sun, J. Zhang, M. Zhang, M. Antonietti, X. Fu, X. Wang, Nat. Commun. 3 (2012) 1132–1139.

[3] Xinchen Wang, Xiufang Chen, Arne Thomas, Xianzhi Fu, and Markus Antonietti, Adv. Mater. 21 (2009) 1609–1612

[4] Mo Zhang, Xiaojuan Bai, Di Liu, Jun Wang, Yongfa Zhu, Appl. Catal. B. 164 (2015) 77–81.

[5] G Liu, P. Niu, C. Sun, S.C. Smith, Z. Chen, G.Q. Lu, H.M. Cheng, J. Am. Chem. Soc. 132 (2010) 11642–11648.

[6] Guigang Zhang , Mingwen Zhang , Xinxin Ye , Xiaoqing Qiu , Sen Lin , Xinchen Wang, Adv. Mater. 26 (2014) 805–809.

[7] Yun Zheng, Lihua Lin, Xiangju Ye, Fangsong Guo, and Xinchen Wang, Angew. Chem. Int. Ed. 53 (2014) 11926 –11930.

[8] Huanxin Zhao, Hongtao Yu, Xie Quan, Shuo Chen, Huimin Zhao, Hua Wang, RSC Adv, 4 (2014) 624-628.

[9] Hua Wang, Yan Su, Huanxin Zhao, Hongtao Yu, Shuo Chen, Yaobin Zhang, and Xie Quan, Environ. Sci. Technol 48 (2014) 11984 −11990

[10] Jinshui Zhang, Mingwen Zhang, Sen Lin, Xianzhi Fu, Xinchen Wang, Journal of Catalysis 310 (2014) 24–30

[11] Wanjun Wang, Jimmy C. Yu, Dehua Xia, Po Keung Wong, and Yecheng Li, Environ. Sci. Technol. 47 (2013) 8724 −8732.

[12] Yu Peng Yuan, Shao-Wen Cao, Yu Sen Liao, Li-Sha Yin, Can Xue, Applied Catalysis B: Environmental 140–141 (2013) 164–168.

[13] Menny Shalom, Miguel Guttentag, Christian Fettkenhauer, Sahika Inal, Dieter Neher, Antoni Llobet, and Markus Antonietti, Chem. Mater, 26 (2014) 5812–5818.

[14] Fan Dong, Zaiwang Zhao, Ting Xiong, Zilin Ni, Wendong Zhang, Yanjuan Sun, and Wing-Kei Ho, ACS Appl. Mater. Interfaces 5 (2013) 11392 −11401.

[15] Gaozu Liao, Shuo Chen, Xie Quan, Hongtao Yu and Huimin Zhao, J. Mater. Chem, 22 (2012) 2721–2726.

[16] Santosh Kumar, T. Surendar, Arabinda Baruahb, Vishnu Shanker, J. Mater. Chem. A, 1 (2013) 5333–5340.

[17] Shifu Chen, Yingfei Hu, Sugang Meng, Xianliang Fu, Applied Catalysis B: Environmental 150–151 (2014) 564–573

[18] Jiye Zhang, Yonghao Wang, Jian Jin, Jun Zhang, Zhang Lin, Feng Huang, Jiaguo Yu, ACS Appl. Mater. Interfaces, 5 (2013) 10317–10324.

[19] Yajun Wang, Rui Shi, Jie Lin and Yongfa Zhu, Energy Environ. Sci. 4 (2011) 2922–2929.

[20] Fan Dong, Zaiwang Zhao, Ting Xiong, Zilin Ni, Wendong Zhang, Yanjuan Sun, and Wing-Kei Ho, ACS Appl. Mater. Interfaces, 5 (2013) 11392 −11401.
[21] Jinshui Zhang, M ingwen Zhang, Rui-Qing Sun, and Xinchen Wang, Angew. Chem. Int . Ed. 51 (2012) 10145 –10149.
[22] Daimei Chen, Kewei Wang, Wangzhi Hong, Ruilong Zong, Wenqing Yao,Yongfa Zhu, Applied Catalysis B: Environmental 166–167 (2015) 366–373.
[23] Huanxin Zhao, Hongtao Yu, Xie Quan, Shuo Chen, Yaobin Zhang, Huimin Zhao, Hua Wang, Applied Catalysis B: Environmental 152–153 (2014) 46–50.
[24] Sheng Chu, Ying Wang, Yong Guo, Jianyong Feng, Cuicui Wang, Wenjun Luo, Xiaoxing Fan, and Zhigang Zou, ACS Catal. 3 (2013) 912 −919.
[25] Sheng Chu, Ying Wang, Cuicui Wang, Juncheng Yang,Zhigang Zou, International journal of hydrogen energy, 38 (2013) 10768 −10772.
[26] Xinguo Ma, Yanhui Lv, Jing Xu, Yanfang Liu, Ruiqin Zhang, Yongfa Zhu, J. Phys. Chem. C 116 (2012) 23485.
[27]Qiaoliang Bao, Bee Min Goh, Bin Yan, Ting Yu, Zexiang Shen, Kian Ping Loh, Adv. Mater. 22 (2010) 3661 – 3666.
[28] Lin Xue, Yanfeng Wang, Yanli Chen, Xiyou Li,J. Colloid Interface Sci. 2010, 350, 523 – 529.
[29] Xiaojuan Bai, Li Wang, Yajun Wang, Wenqing Yao, Yongfa Zhu, Applied Catalysis B: Environmental 152–153 (2014) 262–270.
[30] Park S J, Li K, Jin F L, Mater. Chem. Phys. 108 (2008) 214−219.
[31] Cuicui Wang, Yong Guo, Yu Yang, Sheng Chu, Chenkun Zhou, Ying Wang, Zhigang Zou, ACS Appl. Mater. Interfaces, 5 (2014) 4321–4328.
[32] Aliaksandr Marchanka, Stefan K. Maier, Sigurd Höger, Maurice van Gastel, J. Phys. Chem. B 115 (2011) 13526–13533.
[33] Shunichi Fukuzumi, Hiroaki Kotani, Kei Ohkubo, Seiji Ogo, Nikolai V Tkachenko, Helge Lemmetyinen, J. Am. Chem. Soc. 126 (2004) 1600–1601.